Microstructural, optical, and impedance studies of porous Mn-α-Fe_2O_3/CuO/Ag heterostructures grown using solution-based methods

Pannan I. Kyesmen[12*], Nteseng D. M. Mosalakgotla[1], Adedapo O. Adeola[3], Peverga R. Jubu[2], Philip Omolaye[4], Ahemen I.[2], and Mmantsae Diale[1*]

[1]*Department of Physics, University of Pretoria, Private Bag X20, Hatfield 0028, South Africa.*

[2]*Department of Physics, Joseph Sarwuan Tarka University Makurdi (formerly, University of Agriculture Makurdi) P.M.B. 2373, Makurdi, Benue State, Nigeria.*

[3]*Department of Chemical Sciences, Adekunle Ajasin University, PMB 001, Akungba-Akoko, Ondo-State, Nigeria.*

[4]*Department of Electrical and Electronics Engineering, Joseph Sarwuan Tarka University Makurdi (formerly, University of Agriculture Makurdi) P.M.B. 2373, Makurdi, Benue State, Nigeria.*

Corresponding author's e-mail address: pannan.kyesmen@tuks.co.za: mmantsae.diale@up.ac.za

Abstract

Here, thin films of porous Mn-α-Fe_2O_3/CuO/Ag were prepared; engaging solely low-cost solution-based methods. The dip-coating of CuO on electrodeposited Mn-α-Fe_2O_3 samples using a 180-day-old Cu-based precursor produced films with inhomogeneous morphology and shallow surface pores. This morphology provided the platform for the drop-casting of Ag nanoparticles on the film's surface to form porous Mn-α-Fe_2O_3/CuO/Ag heterostructures. EDS, XRD, and Raman spectroscopy studies affirmed the film's structural integrity. The bandgap estimated for the Mn-α-Fe_2O_3/CuO/Ag samples was 3.8 % less than the values deduced for Mn-α-Fe_2O_3 films. Mott-Schottky analysis disclosed n-type semiconducting behaviour for the Mn-α-Fe_2O_3 films, which was retained after forming heterostructures with CuO and CuO/Ag. The charge transfer resistance at Mn-α-Fe_2O_3/CuO/Ag film's surface in an electrochemical system was 27 times lower than the

approximate values obtained for Mn-α-Fe_2O_3 samples. This research introduces a facile and low-cost approach for fabricating porous Mn-α-Fe_2O_3/CuO/Ag heterostructures with improved properties for photo-base and optoelectronic applications.

Keywords: α-Fe_2O_3-based heterostructures, Thin films, Solution-based methods, Microstructure, Optical properties, Impedance studies.

1.1 Introduction

Hematite (α-Fe_2O_3) is the most popular crystal phase of the oxides of iron (Fe): the fourth most abundant element in the earth's crust [1]. α-Fe_2O_3 is an n-type semiconductor that is thermodynamically stable, non-toxic, abundant, easy and cheap to process, and has a bandgap of ~2.0 eV [2, 3]. These properties make hematite attractive for application in the areas of corrosion control [4], medicine [5], and other optoelectronic applications such as gas sensing [6], photoelectrocatalysis [7], and photovoltaic [8] among others. However, the limitations of α-Fe_2O_3 in many photo-based and optoelectronic applications include its poor conductivity, poor charge transfer kinetics, short diffusion length, and inefficient charge separation [9, 10]. Many concepts have been engaged towards enhancing the intrinsic properties of hematite and mitigating hematite's limitations in many applications. These concepts include doping [11], nanostructuring [12], heterojunction formation [13], and surface modification [14].

Many of the concepts employed in mitigating the challenges of using hematite in many applications contribute in one or more ways toward promoting its properties for improved performance. Doping of α-Fe_2O_3 with materials such as Mn [11], Sn [15], and Ti [16] have been widely employed to improve its conductivity and performance in many applications. Mn-doping of hydrothermally fabricated α-Fe_2O_3 photoanodes has been reported to enhance its conductivity,

resulting in a 75% improvement in photocurrent at 1.23 V vs. reversible H_2 electrode (RHE) when applied in photoelectrocatalysis [11]. Nanostructuring of α-Fe_2O_3-based materials has promoted charge separation on their surfaces, especially in photo-based and optoelectronics applications. The shape of nanostructured α-Fe_2O_3 materials such as nanoparticles [17], nanoflowers [12], and nanorods [18], have been shown to have played a key role in improving the separation of charge carriers in catalytic applications. The fabrication of a heterojunction structure of α-Fe_2O_3 with other semiconductor materials such as TiO_2 [19], CuO [20], and ZnO [13] has been fabricated largely to limit charge recombination and promote its separation in various applications. Mei *et al*. 2022, constructed a α-Fe_2O_3/TiO_2 sensor that exhibited a promising ethanol selectivity, achieving a large response of 40.4 toward 500 ppm ethanol [19]. Also, surface modification of hematite with plasmonic metals such as Au, Ag, and Cu has been used to boost the performance of α-Fe_2O_3-based materials in many photo-based applications by maximizing the effects of localized surface plasmon resonance (LSPR) [21, 22]. These concepts can each address specific aspects of hematite's limitations for improved device performance in many applications. However, a synergy can be attained by systematically engaging the different concepts, to harness their advantages through the fabrication of heterostructures to enhance material properties for various applications. For example, a photocurrent density of 4.68 A/cm2 at 1.23 V vs. RHE (reversible H_2 electrode) has been attained by α-Fe_2O_3/Au/Co-Pi heterostructured photoanodes, which is among the best values reported for α-Fe_2O_3-base materials in photoelectrocatlytic water splitting [23].

Nanostructured heterostructures of hematite-based materials can be fabricated using various methods, including solution-based methods [24-27], resistive evaporation, magnetron sputtering, and chemical vapor deposition, among other techniques [28]. Solution-based methods such as

electrodeposition, dip-coating, drop-casting, and spray pyrolysis are easy and low-cost routes for fabricating nanostructured materials [29, 30]. The drop-casting technique is widely employed for the deposition of plasmonic metals on heterostructured materials [31-33]. However, the deposition of metal nanoparticles with porous surfaces using this technique is challenging because of the high reduction potential of the precursors [34] and the tendency to form compact and aggregated particles [35]. The fabrication of porous surfaces of hematite-based heterostructures provides a larger surface area that promotes charge carriers' separation and device performance in many photo-based [36] and gas sensing [35] applications. This is in addition to an in-built electric field that could be created at the junction between the semiconducting materials of the heterostructure, which can further boost charge transport and separation. So, developing systematic low-cost synthesis strategies for fabricating porous α-Fe_2O_3-based heterostructures will advance their application in many fields.

In this research, concepts, such as nanostructuring, doping, heterojunction formation, and plasmonic enhancement for boosting materials properties in many applications were employed in developing Mn-α-Fe_2O_3/CuO/Ag heterostructures, using facile solution-based methods. Microstructural, optical, and impedance studies were conducted on the heterostructured materials to obtain fundamental insight into their properties. This work provides a facile and low-cost route for fabricating porous Mn-α-Fe_2O_3/CuO/Ag heterostructures with suitable properties for application in photoelectrocatalysis, photovoltaic, gas sensing, and other optoelectronic systems.

1.2 Experimental

1.2.1 Preparation of Mn- α-Fe_2O_3

The electrolyte solution engaged in a previous study to produce α-Fe_2O_3 films via the electrodeposition method [37] was modified with PEG to act as a capping agent and Mn ion doping source. The modified solution was engaged to fabricate Mn-doped α-Fe_2O_3 films on cleaned FTO substrates. The FTO substrates were cleaned using the procedure described in a previous project [38]. In brief, an electrolyte made of 5 mM $FeCl_3$ + 0.1 M KCl + 5 mM KF + 1 M H_2O_2 dissolved in deionized (DI) water was modified with 10% PEG and 3% of $MnCl_2.4H_2O$ by percentage molarity of $FeCl_3$. The resulting solution served as the electrolyte for the electrodeposition of Mn-α-Fe_2O_3 films in a standard three-electrode electrochemical system. The fabricated films, a 2×2 cm mesh of platinum and Ag/AgCl (silver/silver chloride) immersed in 3 M KCl served as the working, counter, and reference electrodes respectively. The distance between the working and counter electrode was 1.2 cm. A VersaSTAT 3F potentiostat was used for the electrodeposition process and the cyclic voltammetry method was engaged within the potential window of -0.5 and 0.5 V vs Ag/AgCl and 60 deposition cycles. This resulted in the deposition of Mn-modified iron oxyhydrate (FeOOH) films on FTO, which were cleaned with DI water to remove possible residual materials. The films were heated to 550 ºC in a furnace at a heating rate of 10°C/min, sintered for 2 hr at that temperature, and left to cool to 25 ºC to get Mn-doped α-Fe_2O_3 films. **Fig. 1(a)** presents a schematic diagram that illustrates the fabrication process of Mn-doped α-Fe_2O_3 films. For comparative and detailed analytical purposes, pristine hematite films were prepared following the same process as Mn-doped samples, except that the Mn ion source was not added to the electrolyte.

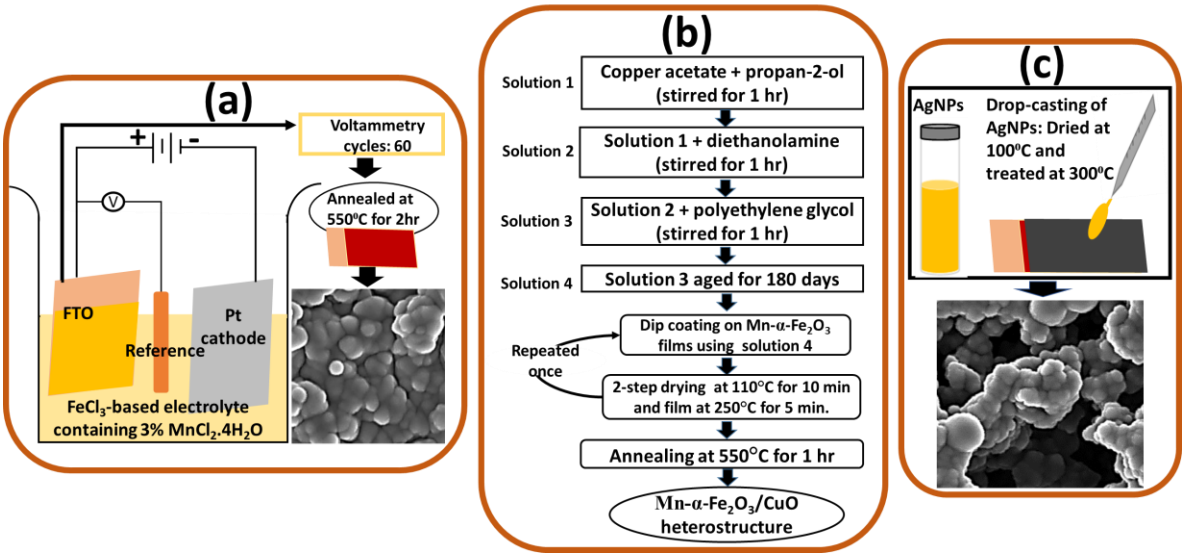

Fig. 1. Schematic summary of the preparation process of (a) Mn-α-Fe_2O_3 films on FTO, (b) CuO on Mn-α-Fe_2O_3 to form Mn-α-Fe_2O_3/CuO, and (c) AgNPs on Mn-α-Fe_2O_3/CuO to obtain Mn-α-Fe_2O_3/CuO/Ag heterostructures.

1.2.2 Preparation of Mn-α-Fe_2O_3/CuO

CuO films were deposited on the Mn-α-Fe_2O_3 samples using an aged Cu-based precursor, in a solution-based dip-coating process, and treated using a three-step heating approach. This was in line with a similar approach introduced in our previous study [39]. Briefly, 27 ml of propan-2-ol was used to dissolve 1.36 g of copper acetate and stirred for 1 hr at 25 ºC. After that, 1.5 ml of diethanolamine was added dropwise into the mixture and stirred for 1hr. Subsequently, 1.5 ml of PEG 400 was added to the solution and stirred for another 1 h. The obtained mixture was aged for 180 days and engaged as the precursor for the fabrication of CuO films on Mn-α-Fe_2O_3 samples via the dip-coating process. The dip-coating process was conducted with a PTL-MM01 dip-coater at 150 mm/min withdrawal velocity. The dip-coated samples were dried at 110 °C for 10 min, then heated to 280 °C and treated at that temperature for 5 min. The dip-coating and drying process was

repeated for a second time to achieve 2 layers of the films. The deposited films were then calcined at 600 °C for 1 hr in air, and left to cool to 25 ºC to obtain crystallized Mn-α-Fe_2O_3/CuO films. **Fig. 1(b)** gives a schematic illustration of the fabrication process of CuO films on Mn-doped α-Fe_2O_3 samples. For comparison and detailed analytical studies, pristine CuO films made of 2 layers were deposited on FTO substrates, following the same procedure used to prepare the samples on Mn-α-Fe_2O_3.

1.2.3 Preparation of Mn- α-Fe_2O_3/CuO/Ag

Ag NPs were deposited on Mn-α-Fe_2O_3/CuO samples using the drop-casting method. First, 50 ml of 1 mM of Silver Nitrate ($AgNO_3$) was prepared in di-ionized (DI) water under vigorous stirring, at room temperature. The gradual addition of 1 mM trisodium citrate ($Na_3C_6H_50_7$) into the solution was done while stirring. Lastly, 1.5 ml of aqueous solution of 40 mM Sodium Borohydride ($NaBH_4$) was added to the solution, which immediately turned yellow. The heat treatment of the mixture was then done at 100 °C for 30 min to obtain a solution of Ag NPs which was used for the drop-casting of Ag on Mn-α-Fe_2O_3/CuO samples [40]. For the deposition of the metallic Ag, 150 µL of the Ag NPs solution was deposited dropwise on the Mn-α-Fe_2O_3/CuO films in a drop-casting method and allowed to dry at 100 °C for 15 min. The drop-casting process was repeated once to increase the Ag NPs loading on the samples. The samples were further treated in a furnace at 300 ºC for 10 mins under an inert atmosphere of N_2 gas to obtain Mn-α-Fe_2O_3/CuO/Ag samples. **Fig. 1(c)** shows a summary of the drop-casting process for the deposition of Ag NPs on Mn-α-Fe_2O_3/CuO in a schematic diagram. The same process was engaged to deposit Ag NPs on FTO/CuO samples for comparison and detailed analytical purposes.

1.2.4 Samples characterization

Using the Ultrafast 540 equipment, field emission gun scanning electron microscopy (FEG-SEM) analysis was conducted on the fabricated α-Fe_2O_3-based samples to examine their surface and cross-sectional morphologies. The FEG-SEM apparatus was attached to an EDS setup, which was used to perform elemental composition mapping and point measurements on the sample's surfaces. A Bruker D2 PHASER-e diffractometer with Cu-Kα radiation of 0.15418 nm wavelength was engaged to perform XRD measurements on the fabricated samples to gain insight into their structural characteristics. The prepared samples were further analysed using the Raman spectroscopy technique via a WiTec alpha300 RAS+ Confocal Raman Microscope with a 532 nm laser at 5 mW. The optical characteristics of the fabricated α-Fe_2O_3-based samples were investigated using an Agilent CARY 60 UV-Vis (Ultraviolet-Visible) spectrometer.

1.2.5 Electrochemical impedance measurements

Impedance measurements, including Mott-Schottky (M-S) and electrochemical impedance spectroscopy (EIS), were performed on the Mn-α-Fe_2O_3, Mn-α-Fe_2O_3/CuO, Mn-α-Fe_2O_3/CuO/Ag samples using the VersaSTAT 3F potentiostat from Princeton Applied Research. The electrolyte used for the measurements was 1 M NaOH, and a 22 cm platinum mesh, Ag/AgCl in a 3M solution, and the prepared films were engaged as the counter, reference, and working electrodes respectively. The M-S measurements were done in dark conditions at 1000 Hz and 10 mV AC potential amplitude in a DC potential window of -1.1 to 0.6 V vs. Ag/AgCl. The EIS measurements were also conducted on the working electrodes in dark conditions at 0.4 V vs Ag/AgCl, a frequency range of 10000 to 0.1 Hz, and a 10 mV AC potential amplitude. The data collected from the raw EIS measurements were fitted to a modeled equivalent circuit using the EIS Spectrum Analyser software. The reference potentials against Ag/AgCl were converted to the reversible hydrogen electrode (RHE) using the Nernst equation given in previous work [41].

1.3 Results and Discussion

1.3.1 Surface morphology

The surface microstructures of the α-Fe_2O_3-based films were investigated to study the surface properties of the heterostructured materials. The surface micrographs of the samples are shown in **Fig. 2(a), (b), (c),** and **(d)** for pristine α-Fe_2O_3, Mn-doped α-Fe_2O_3, α-Fe_2O_3/CuO, and α-Fe_2O_3/CuO/Ag films respectively. The histogram of the particle size distribution used to approximate the mean value of the film's particles is given in the insets of the micrographs for each of the sample's surface images, respectively. All the fabricated composite materials that formed the heterostructure disclosed spherical nanoparticles with some particle agglomeration. The morphology of the pristine α-Fe_2O_3 films was not affected by Mn-doping as both samples reveal slightly agglomerated spherical nanoparticles. However, the estimated mean particle size of the α-Fe_2O_3 films reduces by 20.0% after Mn-doping, yielding a value of 26.0 nm with a standard deviation (SD) of 5.1. The reduction in particle size shows that Mn-doping has an inhibiting impact on the particle's growth and the nucleation of hematite, which is similar to previous observations [42, 43]. The deposition of CuO on the Mn-α-Fe_2O_3 samples using the 180-day-old aged precursors produced shallow pores on the film's surface consisting of nanoparticles with a mean size of 25.2 nm and SD value of 6.4. The precursor aging led to the replacement of the acetate in the initial solution containing Cu-acetate with the more elongated ligands of diethanolamine. The elongated ligands formed in the aged precursor induced the porosity observed on the surface of the α-Fe_2O_3/CuO heterostructures, similar to previous reports [39, 44]. An additional explanation of the ligand transformation process is given in section 1.3.3. The pores on the surface of the Mn-α-Fe_2O_3/CuO films provided the platform for the growth of porous AgNPs. The pores on the heterostructure's surface were significantly sustained after its surface modification with Ag NPs.

The Ag NPs revealed some agglomeration at the film's surface with an approximate mean particle size of 20.5 nm and SD value of 5.5. For reference purposes, a wider view of the surface micrographs of the fabricated samples obtained at lower magnifications is disclosed in **Fig. S1(a) - (d)** of the supplementary document.

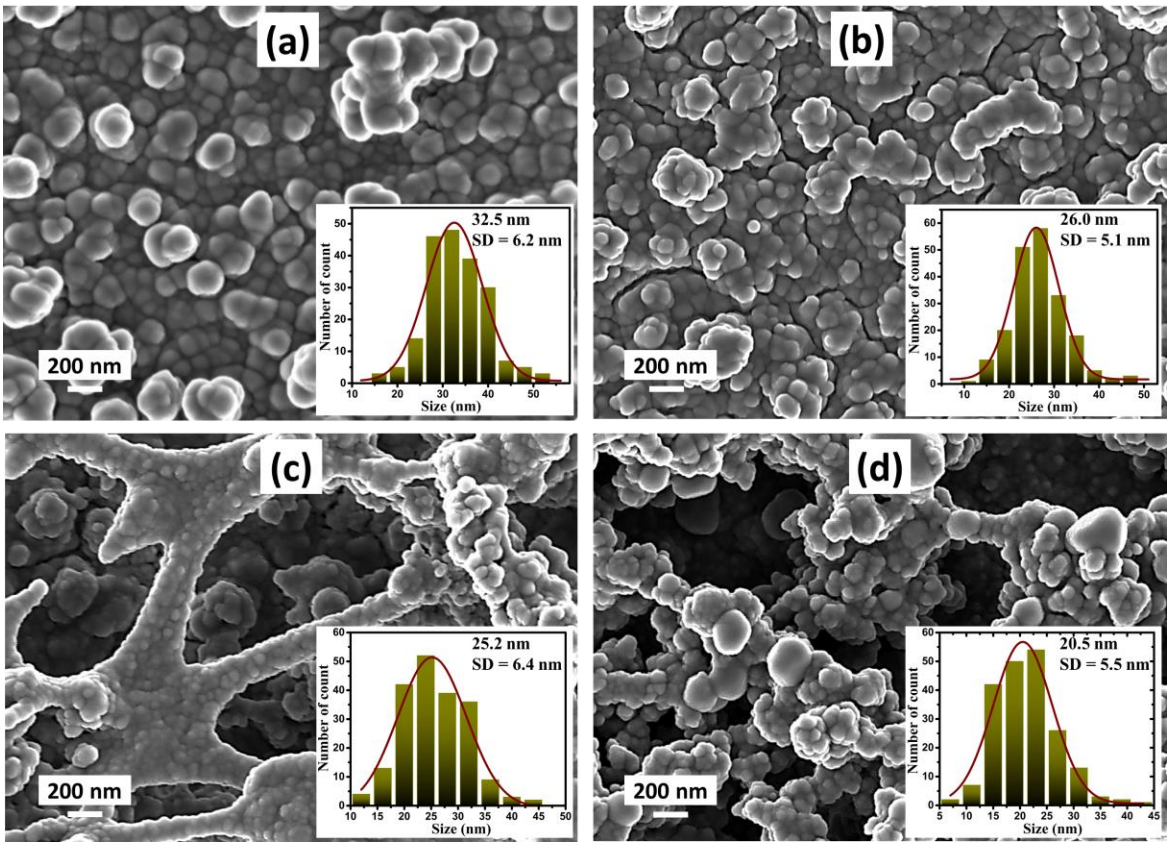

Fig. 2. The SEM micrographs of (a) pristine α-Fe_2O_3, (b) Mn-doped α-Fe_2O_3, (c) α-Fe_2O_3/CuO, and (d) α-Fe_2O_3/CuO/Ag films.

To further prove that the pores on the surface of α-Fe_2O_3/CuO provided the platform for the growth of porous Ag NPs on the film's surface, the SEM images of CuO prepared using a 1-day-old Cu-acetate precursor, CuO-1d, and CuO-1d/Ag NPs is presented in **Fig. S2**. The CuO-1d and CuO-1d/Ag NPs disclosed compact nanoparticles with no pores on the surfaces of both films. This

affirms that the pores on the surface of the CuO films prepared using the 180-day-old Cu-based precursor catalyzed the formation of porous α-Fe_2O_3/CuO/Ag.

The porous surface obtained for the samples is desired for many photo-based and optoelectronic applications. However, the high particle aggregates observed on the sample's surface can negatively impact charge transport and separation in many applications. So, it will be beneficial to devise means of limiting the aggregation of the nanoparticles. The Ag NPs can boost the performance of the heterostructure in many fields by taking advantage of its plasmonic effects. Since Ag is a plasmonic metal, it can form LSPR at the surface of the heterostructures and promote its performance in many applications such as gas sensing, photoelectrocatalysis, and photovoltaics through the injection of hot-electrons, enhanced scattering of light, and resonant energy transfer [22].

The SEM image of the cross-section of the Mn-α-Fe_2O_3/CuO/Ag sample is presented in **Fig. 3**. The image was analyzed using the ImageJ tool to evaluate the thickness of each of the layers of the deposited films. Film thicknesses of 330 ± 40, 153 ± 30, and 86 ± 18 nm were deduced for the Mn-α-Fe_2O_3, CuO, and Ag layers of the heterostructure respectively. The total thickness of 569 ± 42 nm deduced for the heterostructure will be suitable for its application in photo-based systems such as photoelectrocatalysis. This is because α-Fe_2O_3 needs films with thickness of about 400-500 nm for sufficient photon absorption due to its low absorption coefficient [45]. For other optoelectronic applications, the thickness of the different layers of the heterostructure will need to be appropriately optimized. A clear distinction is visible between the Mn-α-Fe_2O_3 and CuO layers of the heterostructure, which suggests the creation of a p-n heterojunction between them. The p-n junction created can result in the development of an in-built electric field at the interface between

the materials, which will help boost charge transport in many electronic and photo-based applications [46].

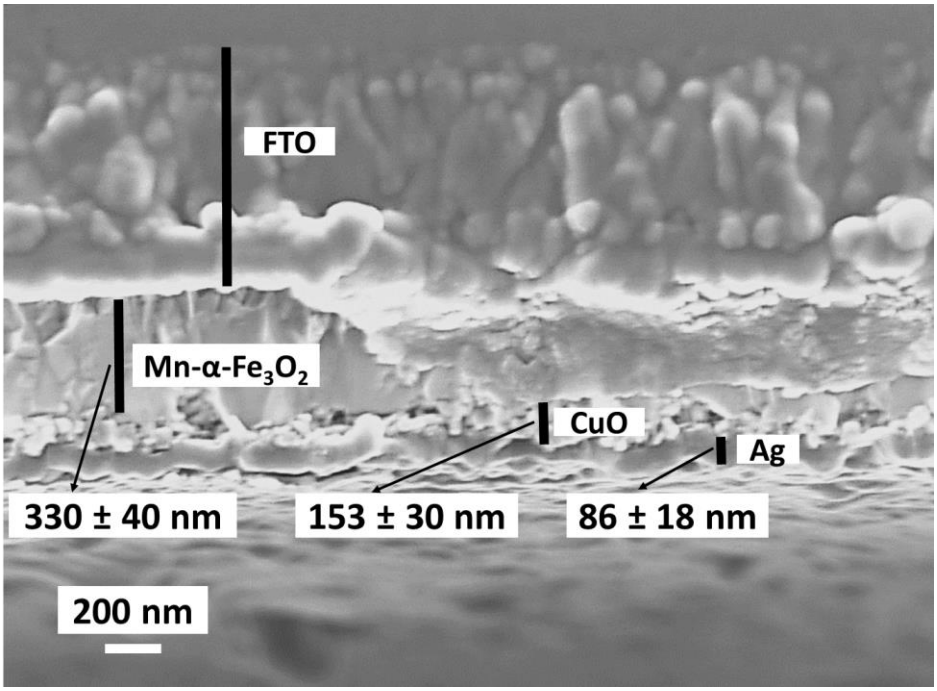

Fig. 3. SEM cross-sectional morphology of Mn-α-Fe_2O_3/CuO/Ag.

EDS mapping was conducted on the surface of Mn-α-Fe_2O_3/CuO and Mn-α-Fe_2O_3/CuO/Ag films to evaluate the various compositional elements that are part of the heterostructure and the maps obtained are displayed in **Fig. 4(a)** and **(b)** respectively. The mapping done on α-Fe_2O_3/CuO samples affirms the presence of Fe, O, Cu, Mn, and Sn, which are uniformly distributed across the film's surface. The O content observed results from the various composites of metal oxides in the heterostructure. The Fe and Cu constituents detected resulted from the content of α-Fe_2O_3 and CuO of the composite materials, while the presence of Mn provides evidence of Mn-doping of α-Fe_2O_3. The dark regions on the EDS map of the films are the shallow areas formed by the inducement of porosity on the film's surface that resulted from the deposition of CuO on Mn-α-Fe_2O_3. The EDS mapping performed on Mn-α-Fe_2O_3/CuO/Ag samples also detected all the elements observed for

Mn-α-Fe_2O_3/CuO and the presence of Ag, which is expected after the deposition of Ag NPs on the films. The presence of unwanted materials was not detected in the EDS mapping, which indicates good purity of the fabricated heterostructures. To further confirm the purity of the heterostructures, EDS point analysis was performed on Mn-α-Fe_2O_3/CuO/Ag sample, and the result is presented in **Fig. 4(c)**. The result affirmed all the constituent elements observed in the EDS mapping of the sample and no impurities were detected.

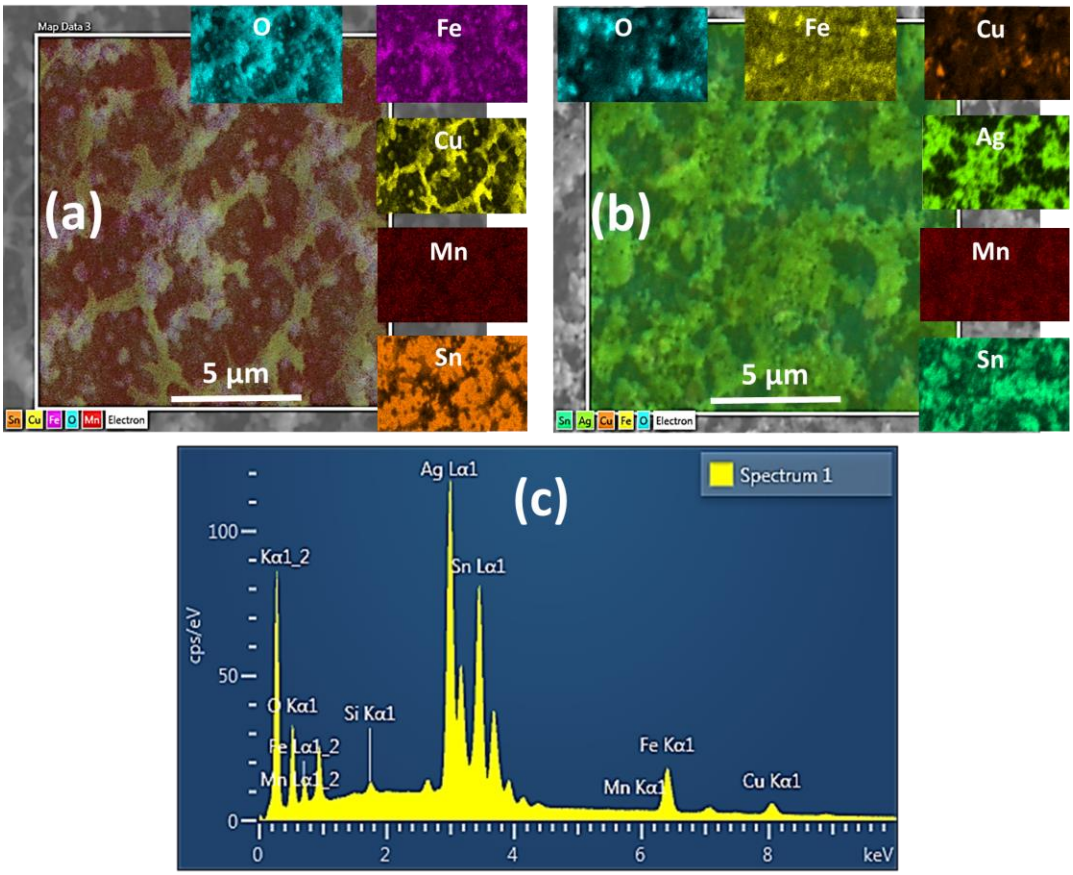

Fig. 4. The EDS maps of (a) Mn-α-Fe_2O_3/CuO and (b) Mn-α-Fe_2O_3/CuO/Ag films while (c) shows the point analysis for Mn-α-Fe_2O_3/CuO/Ag heterostructure.

1.3.2 Structural studies

XRD analysis was conducted on the fabricated samples to gain insight into the structural characteristics of the films. **Fig. 5** displays the XRD patterns for Mn-α-Fe_2O_3, Mn-α-Fe_2O_3/CuO, and Mn-α-Fe_2O_3/CuO/Ag samples. The pattern observed for the Mn-α-Fe_2O_3 films produced XRD peaks at (104) and (110) planes, which affirm the rhombohedral structure for crystallized α-Fe_2O_3, having lattice parameters of a = b = 5.032, c = 13.733; and $R\bar{3}c$ space group. Other weak XRD peaks were seen at (012), (113), (024), (168), (018), (214), and (310) planes for the Mn-α-Fe_2O_3 samples, which is attributed to those of α-Fe_2O_3 in line with the JCPDS file no. 33-0664. The diffraction pattern of Mn-α-Fe_2O_3/CuO disclosed additional peaks at ($\bar{1}11$) and (111) planes which are ascribed to the monoclinic crystal structure of CuO with lattice indices of a = 4.64 Å, b = 3.4 Å, c = 5.09 Å, β = 99.5° based on the JCPDS file number 05-0661. The peak at the ($\bar{1}11$) plane observed in the heterostructure for CuO overlapped with that of (110) of α-Fe_2O_3. This is more visible in the XRD pattern of the pristine CuO films given in **Fig. S3** of the supplementary data. For Mn-α-Fe_2O_3/CuO/Ag films, the pattern disclosed more peaks at 2 theta values of 44.3, 64.4, and 77.3º corresponding to the (200), (220), and (311) planes respectively. These correlate to the peaks for the crystalline face-centered, cubic structure of Ag, according to the JCPDS file number 04-0783, and are similar to the peaks observed for AgNPs in a previous study [47]. An expanded view of the XRD pattern of Mn-α-Fe_2O_3/CuO/Ag heterostructure, given in **Fig. S4** shows clearly the observed peaks for AgNPs. A popular XRD peak for AgNPs; the (111) plane at 2 theta value of about 38.1º was not visible because it overlaps with one of the prominent peaks of FTO at that position. The peaks for the oxides of Fe, Cu, and Ag were not detected in all the XRD results, confirming the good purity of the fabricated Mn-α-Fe_2O_3/CuO/Ag heterostructures.

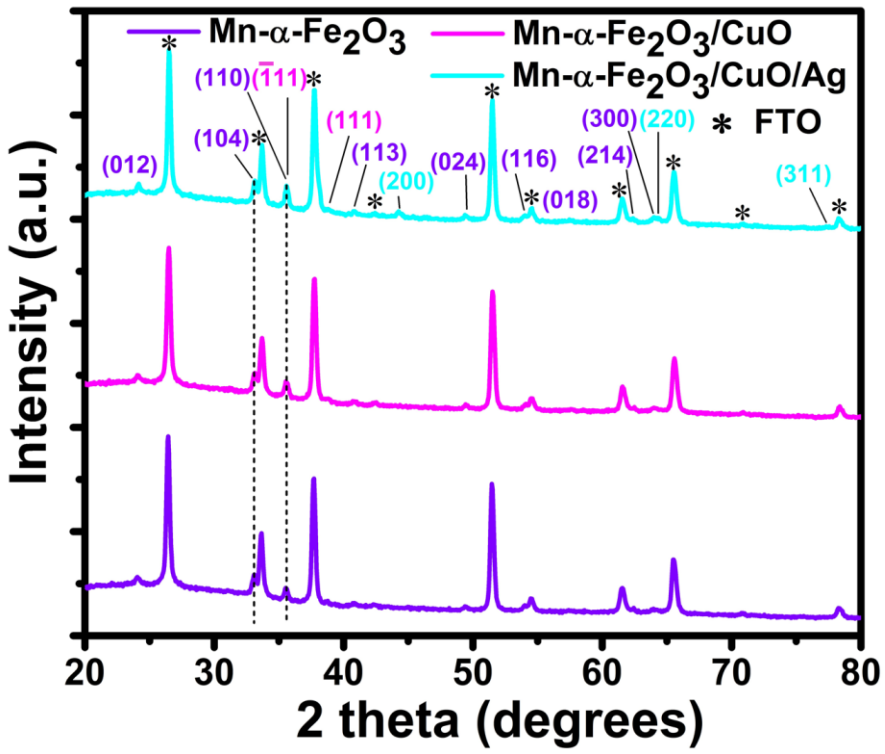

Fig. 5. The XRD patterns for Mn-α-Fe_2O_3, Mn-α-Fe_2O_3/CuO, and Mn-α-Fe_2O_3/CuO/Ag samples.

Fig. S3 of the supplementary data compares the XRD pattern for CuO, α-Fe_2O_3, and Mn-α-Fe_2O_3. The peaks at (111) and ($\bar{1}$11) planes are more visible in the XRD pattern of the pristine CuO films. In the XRD pattern, the same peaks observed for the pristine α-Fe_2O_3 were also detected for the Mn-doped samples, as expected. However, the peak positions shifted to smaller 2 theta values for the Mn-α-Fe_2O_3 samples relative to the observed peaks for the pristine films, with the (104) and (110) planes shifting by 0.263 and 0.264º respectively. This was caused by an increase in the lattice volume of the Mn-doped samples because Mn^{2+} has a greater atomic radius (r = 0.083 nm) [48] than F^{3+} (r = 0.064 nm) [49]. Comparable observations have been reported for α-Fe_2O_3 samples doped with In^{3+} [50] and Cu^{2+} [49]. The peak positions of α-Fe_2O_3 in the XRD patterns of Mn-α-Fe_2O_3, Mn-α-Fe_2O_3/CuO, and Mn-α-Fe_2O_3/CuO/Ag did not yield any noticeable shift (**Fig. 5**),

which suggest that no unintentional doping of Mn-α-Fe_2O_3 by Cu occurs at the annealing stage during the fabrication of Mn-α-Fe_2O_3/CuO films.

The crystal size (D) of the different materials that made up the heterostructure was evaluated using the popular Debye Scherer approximation defined by **Equation 1**:

$$D = \frac{k\lambda}{\mathcal{B}cos\theta} \quad (1)$$

Where the wavelength, λ, is 0.15418 nm, β denotes the full width at half maximum (FWHM), and θ denotes the diffraction angle. The crystal planes at (110) were used to evaluate the D values for α-Fe_2O_3 and Mn- α-Fe_2O_3 while the ones at $(\bar{1}11)$ and (200) were used to estimate the crystallite sizes of CuO and AgNPs respectively. Also, using Williamson and Smallman's approximation, the microstrain (ε) and dislocation density (ɗ) of the samples were evaluated [51]. The results obtained are given in Table S1 of the supplementary document. Crystallite sizes of 27.9 and 25.7 nm were calculated for α-Fe_2O_3 and Mn-α-Fe_2O_3 films respectively. The decreased D value observed for Mn-α-Fe_2O_3 was caused by the difference in the ionic radius of Mn^{2+} and Fe^{3+}, which limits the crystallization of the doped samples [52]. A similar drop in crystallization has been reported for Cu-doped β-Ga_2O_3 [53] and Al-doped ZnO [52]. The crystallite sizes evaluated for CuO films and AgNPs are 20.5 and 18.7 nm respectively. The crystal size values of nanomaterials can play critical roles in different applications. In phototoelectrocatalysis, enhanced crystallization is desired for improved material conductivity and charge separation [54], while smaller crystallites increase grain boundaries and are more beneficial in gas-sensing applications [55]. Therefore, this property can be tailored to suit the application of the heterostructure in different fields. The microstrain of the α-Fe_2O_3 films became larger by 8.1% after Mn-doping due to the replacement of Fe^{3+} with Mn^{2+}. Similarly, the D values increase for the α-Fe_2O_3 films by 17.1% after Mn-

doping. This is because of the enhancement in lattice disorder that results from Mn^{2+} substitution of Fe^{3+}. The ε and ɖ values evaluated for the CuO and Ag films were significantly higher than the ones approximated for both the pristine and Mn-doped α-Fe_2O_3 samples.

For more insight into the structural properties of the heterostructures, Raman spectroscopy studies were done and the results are displayed in **Fig. 6** for CuO/Ag, Mn-α-Fe_2O_3, Mn-α-Fe_2O_3/CuO, and Mn-α-Fe_2O_3/CuO/Ag samples. The Raman spectra of CuO/Ag yielded peaks for two B_g and one A_g vibrational phonon modes of CuO [56]. It also produced a peak at 238 cm^{-1} which is ascribed to the vibrational mode of Ag-O bond stretching [47]. The Raman spectra of Mn-α-Fe_2O_3 disclosed the two A_{1g} and five E_g phonon modes of α-Fe_2O_3. The spectra of Mn-α-Fe_2O_3/CuO, and Mn-α-Fe_2O_3/CuO/Ag films revealed more Raman peaks for the B_g and A_g vibrational modes of CuO. The Raman peak for Ag at 238 cm^{-1} could not be visible in the spectra of the heterostructures because it overlaps with the peak of the first E_g mode observed for Mn-α-Fe_2O_3. The heterostructures did not produce any Raman peak shifts relative to the ones observed for the Mn-α-Fe_2O_3 samples, suggesting that no further doping of α-Fe_2O_3 by Cu^{2+} occurred during sample preparation. The peaks observed for the α-Fe_2O_3-based heterostructures at 557 cm^{-1} are regarded as the LO (longitudinal optical) Eu modes of α-Fe_2O_3, which are infrared active and often activated by occurrences of local disorder and strain within the α-Fe_2O_3 lattice [57]. The intensity of the LO mode peaks appeared to be significant in the Mn-α-Fe_2O_3 films and the fabricated heterostructures due to the Mn-doping of α-Fe_2O_3 which promoted lattice disorder. No additional Raman peaks were observed for any undesired oxides of Fe, Mn, Cu, or Ag, indicating good quality for the prepared heterostructures.

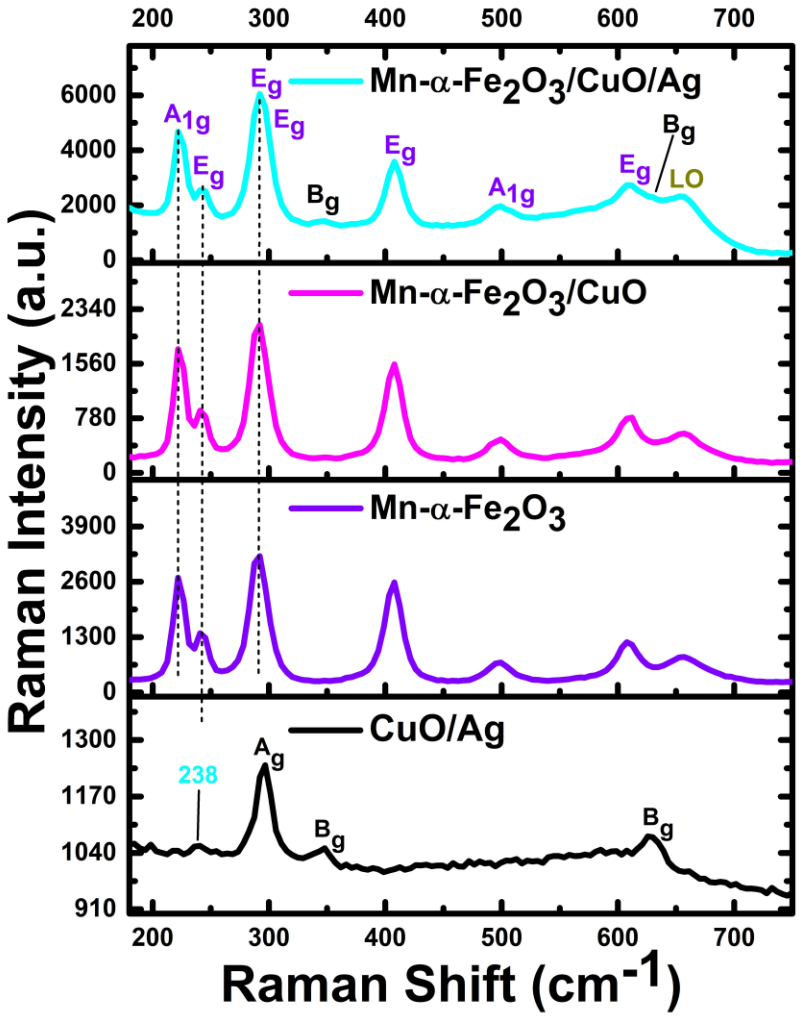

Fig. 6. The Raman spectra of CuO/Ag, Mn-α-Fe_2O_3, Mn-α-Fe_2O_3/CuO, and Mn-α-Fe_2O_3/CuO/Ag films.

1.3.3 Optical characteristics

UV-vis spectroscopy studies were conducted on the fabricated samples to obtain their optical absorption patterns and deduce their approximate direct and indirect bandgaps. The absorption pattern of Mn-α-Fe_2O_3, Mn-α-Fe_2O_3/CuO, and Mn-α-Fe_2O_3/CuO/Ag are displayed in **Fig. 7(a)**. The absorption spectra of the films produced an absorption onset that ranges from 606 to 617 nm with Mn-α-Fe_2O_3 yielding the minimum value. The fabrication of Mn-α-Fe_2O_3/CuO and Mn-α-

Fe_2O_3/CuO/Ag heterostructures boosted the photon absorption of Mn-α-Fe_2O_3 films, increasing its onset absorption by 1.0 and 1.8% respectively. The enhanced light absorption observed for Mn-α-Fe_2O_3/CuO was promoted by the inhomogeneous morphology and the pores on the surface of the samples that boosted light scattering, elongating the travel path of photons [58]. The deposition of AgNPs on the heterostructure further improved photon absorption through the plasmon resonance effects [22]. The film's absorption spectra disclosed absorption transition peaks at 319, 390, and 546 nm wavelengths. The peak at 319 nm is ascribed to the transitions that arise due to the charge transfer from O^{2-} to Fe^{3+}. This depicts the charge transfer between the non-bonding orbitals and the lowest empty orbital [59]. The peaks at 546 and 390 nm relate to the transition ligand fields $^6A_1 - {}^4E_1$, $^4A_1$, associated with a single Fe^{3+} cation and the transitions that occur during double exciton processes between $Fe^{3+} - Fe^{3+}$ ion pairs respectively [60].

The precursor aging of Cu acetate-based precursor induced the formation of the observed porous surfaces of Mn-α-Fe_2O_3/CuO and Mn-α-Fe_2O_3/CuO/Ag heterostructures which consequently contributed to the reduced bandgap deduced for the samples. The aging of the precursor led to a gradual replacement of the acetate ligand ions in the solution with diethanolamine in a slow complexation reaction. A detailed UV-Vis investigation of the initial and aged Cu-based precursors presented in our previous work affirms the creation of bis-(diethanolamine) copper (II) complex in the 180-day-old solution [39]. The diethanolamine complex is a more elongated ligand compared to its acetate counterpart. The longer diethanolamine ligand in the precursor induced the formation of the large pores observed on the surface of Mn-α-Fe_2O_3/CuO samples and consequently on Mn-α-Fe_2O_3/CuO/Ag, similar to previous reports [44, 61].

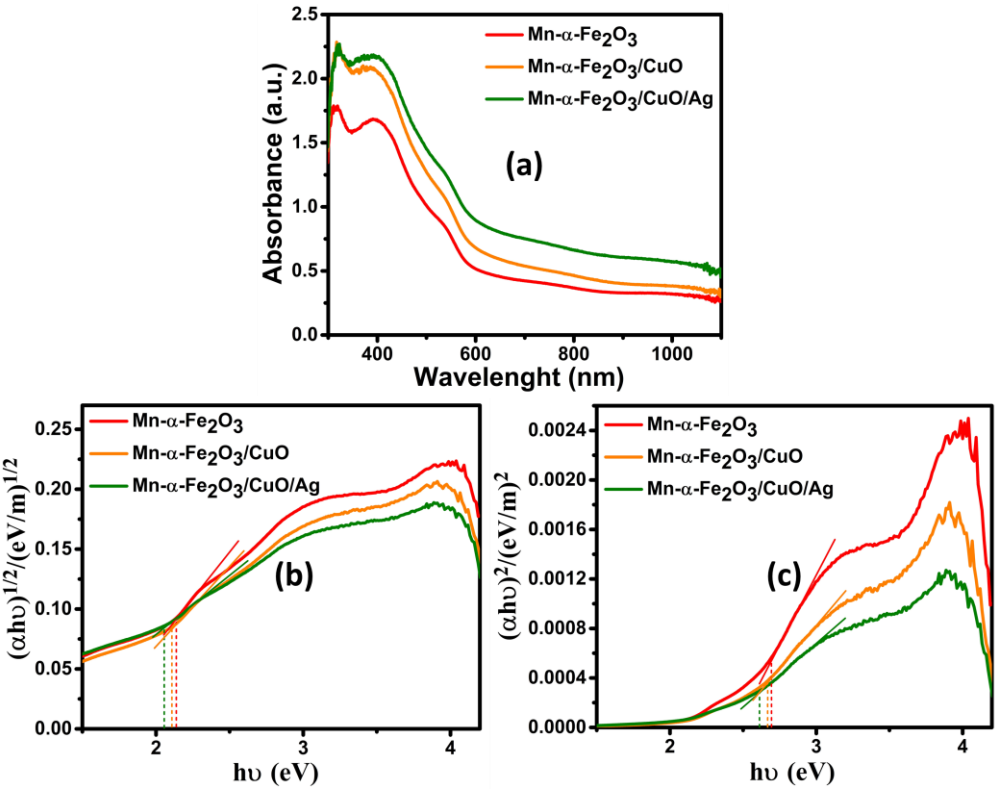

Fig. 7. The (a) UV-Vis absorption pattern, (b) indirect bandgap, and (c) direct bandgap of the fabricated Mn-α-Fe_2O_3 and heterostructured samples, respectively.

Furthermore, the indirect and direct bandgap of the fabricated samples were calculated using the widely engaged Tauc approximation defined by **Equation 2**

$$\alpha h\nu = A\left(h\nu - E_g\right)^s \qquad (2)$$

where h denotes the Planck constant, ν is light's frequency, A is a constant, E_g represents the band gap, and s is a constant which can be 2 for allowed indirect transitions, and 1/2 for direct transitions [62, 63]. The Tauc plots for the indirect and direct optical bandgaps approximation of the films are given in **Fig. 7(b)** and **(c)** respectively. The indirect bandgap deduced for Mn-α-Fe_2O_3, Mn-α-Fe_2O_3/CuO, and Mn-α-Fe_2O_3/CuO/Ag were 2.13, 2.10, and 2.05 respectively. The absorption

onset's red-shifted for the heterostructures relative to Mn-α-Fe_2O_3 films due to improved photon absorption and led to the reduced bandgap values evaluated for the samples. Similarly, the approximated direct bandgaps yielded lower values of 2.67 and 2.61 eV for Mn-α-Fe_2O_3/CuO, and Mn-α-Fe_2O_3/CuO/Ag while Mn-α-Fe_2O_3 yielded 2.70 eV. For many photo-based applications, the decreased bandgap observed for the heterostructures is advantageous as it promotes photon utilization within the visible spectrum, improving the photogeneration of charge carriers and device efficiency [64].

1.3.4 Impedance Studies

Impedance studies were conducted to evaluate some electrical properties of the fabricated materials. The electronic properties of the materials can be obtained by investigating the capacitance of the space charge region, C, in an electrolyte as a function of potential, under the depletion condition. The Mott-Schottky measurements were used for this analysis to obtain the electronic properties of the materials such as the flat band potential V_{fb} and their donor density, N_D. The results obtained from the measurements are shown in the MS plots in **Fig. 8**. The plots show a positive slope for the Mn-α-Fe_2O_3 samples, affirming the n-type semiconducting behaviour of the films. The heterostructures of Mn-α-Fe_2O_3 with CuO and CuO/AgNPs also show a positive slope for the MS plots. This indicates that Mn-α-Fe_2O_3 films retained their n-type semiconducting properties after forming heterostructures with CuO and CuO/AgNPs. This further affirms the successful fabrication of the heterojunction structures since CuO is a p-type material. The MS formula used to evaluate the V_{fb} and N_D of the materials from the plots is given in **Equation 3**:

$$\frac{1}{C^2} = \frac{2}{\varepsilon_0 \varepsilon e A^2 N_D} \left(V - V_{fb} - \frac{KT}{e}\right) \quad (3)$$

Where the capacitance of the space charge layer is given as *C*, *A* is the electrode's surface area, the dielectric constant is denoted as Ɛ and is about 80 for α-Fe_2O_3, the vacuum permittivity is represented by $Ɛ_0$, *e* denotes the electronic charge, *V* represents the applied potential, K denotes the Boltzmann constant, and T symbolizes the temperature [65]. The first linear portions of the MS plots were fitted and the intercepts of the fitting on the V-axis were used to deduce the V_{fb} of the electrodes in line with **Equation 3**. Also, the N_D of the materials was evaluated using **Equation 4**:

$$N_D = \frac{2}{Ɛ_0 Ɛ e A^2} [S^{-1}] \quad (4)$$

Where S represents the slope of the MS plot.

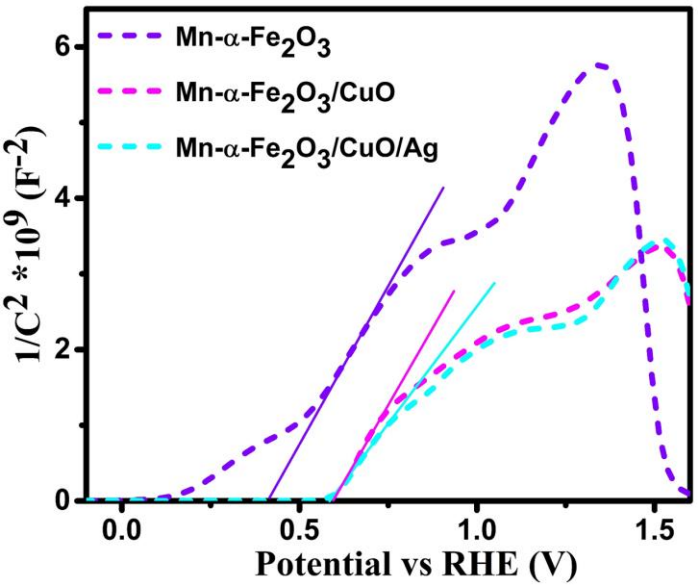

Fig. 8. MS plots for the fabricated Mn-α-Fe_2O_3, Mn-α-Fe_2O_3/CuO, and Mn-α-Fe_2O_3/CuO/Ag films.

The flatband potential evaluated for the Mn-α-Fe_2O_3 films was 0.364 V vs. RHE and more positive potentials were obtained for the heterostructures, yielding values of 0.565 and 0.552 V vs. RHE for Mn-α-Fe_2O_3/CuO, and Mn-α-Fe_2O_3/CuO/Ag electrodes. The positive shift in the V_{fb} values of the heterostructures relative to the estimated value for Mn-α-Fe_2O_3 was due to the equilibration of the fermi levels of Mn-α-Fe_2O_3 and CuO after the heterojunction formation. The Fermi level of CuO is more positive than that of Mn-α-Fe_2O_3. So the development of a heterojunction between these materials will cause the fermi level of the composites to equilibrate and shift to a more positive value relative to that of Mn-α-Fe_2O_3 [66]. Comparable observations have been reported for other heterostructured materials [66, 67]. Meanwhile, the V_{fb} value of Mn-α-Fe_2O_3/CuO/Ag slightly shifted to more negative potential by 13 mV relative to the value evaluated for Mn-α-Fe_2O_3/CuO. This implies an improvement in charge separation, resulting from the effects of plasmon resonance associated with the Ag NPs on the film's surface [68]. For the heterostructures, despite the positive shift in V_{fb} values, the in-built field that will be created at the junction between Mn-α-Fe_2O_3 and CuO will promote the injection of charge carriers to the surface of the films and their separation [46, 68]. This will be suitable for many photo-based applications such as photo-degradation [69], photo-detection [70], and photoelectrocatalysis [68].

The donor density, N_D, estimated for the Mn-α-Fe_2O_3 samples was 7.0 x 10^{-19} cm^{-3}. The N_D increases to 7.3 and 9.6 x 10^{-19} cm^{-3} for Mn-α-Fe_2O_3/CuO and Mn-α-Fe_2O_3/CuO/Ag electrodes respectively. The enhanced donor densities observed for the heterostructures were largely attributed to the reduction in the recombination of charge carriers because of the in-built field created at the junction between the semiconducting materials [71]. Comparable observations where an increase in the N_D values of heterojunction materials have been reported in previous studies [46, 72]. The modification of Mn-α-Fe_2O_3/CuO with AgNPs further boosted the N_D value

by a factor of about 1.3 due to a further decrease in the recombination of charge carriers arising from the plasmonic effects of the metal NPs. Shinde *et al*. 2024, reported a similar observation for a ZnO/CuO/Au NPs heterostructure [68]. An increase in the donor density of the composite materials will provide more electrons in their conduction band. This will improve the conductivity of the films, increasing charge carriers' mobility and transport, which are also desired properties for many photo-based applications.

EIS studies were done to evaluate the charge transport dynamics in the buck and at the surface of the electrodes. The Nyquist plots of the Mn-α-Fe_2O_3 and heterostructures obtained from the EIS measurements are displayed in **Fig. 9 (a)**. The equivalent circuit model used to fit the measured EIS data is shown in the inset of **Fig. 9 (a)**. The circuit consists of a series resistance, Rs, constant phase elements, CPE-1 and CPE-2 to denote the non-ideal capacitance in the bulk and surface of the films respectively. Rbk represents the resistance of the trap states in the bulk of the electrodes and Rct denotes the resistance to charge transfer at the surface of the films. The values obtained for the elements, CPE-1 and -2, which represents the non-ideal capacitance of the materials were used to evaluate the actual capacitance, *C*, of the samples using **Equation 5** [73]:

$$C = Q^{1/n} \times R^{(1-n)/n} \quad (5)$$

Where the resistance connected in parallel to the respective CPE elements is denoted by, *R*, the effective coefficient of the CPE elements is represented by, Q, and *n* denotes their exponent values which could range from 0-1. The symbols C1 and C2 depict the actual capacitance values calculated for the CPE-1 and CPE-2 elements, respectively. All the values obtained for the modeled circuit elements used to fit the EIS data and the parameters evaluated from them are presented in **Table 1.**

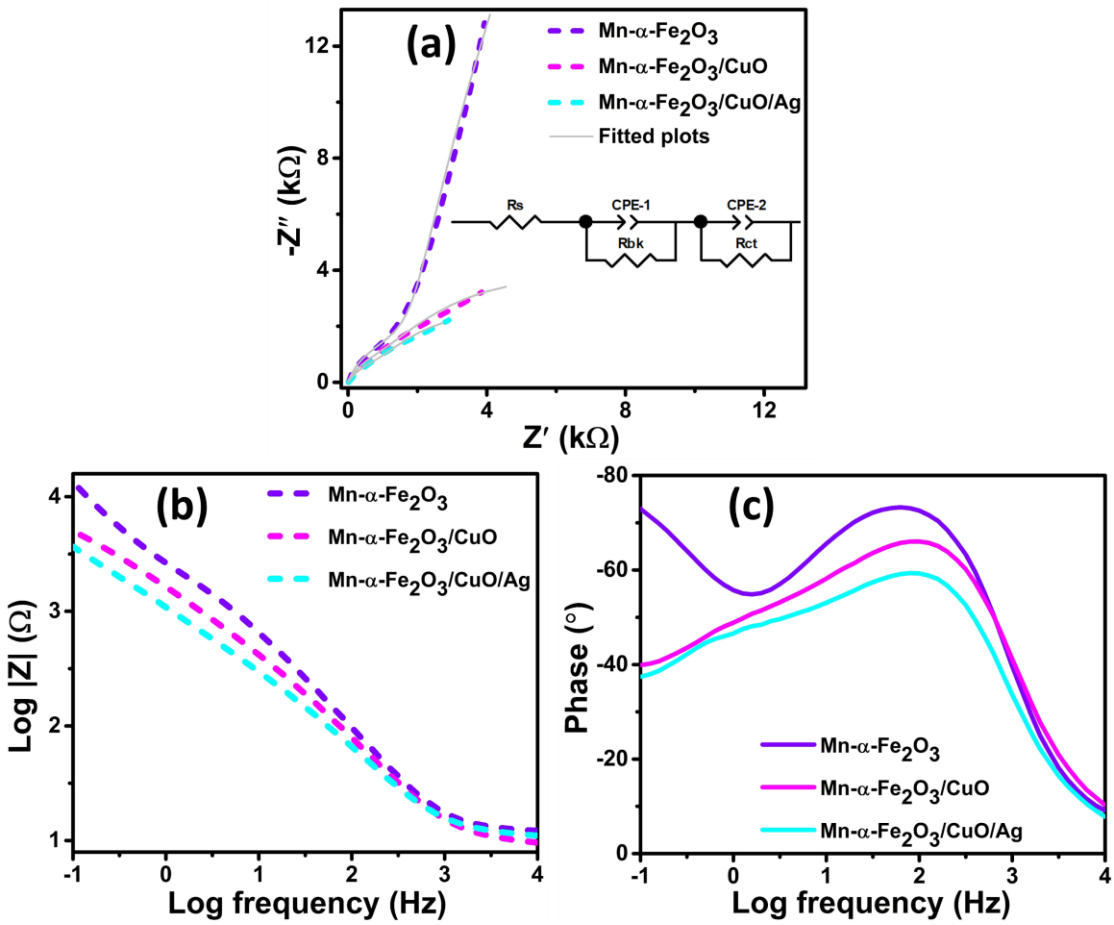

Fig. 9. (a) Nyquist plot of Mn-α-Fe_2O_3, Mn-α-Fe_2O_3/CuO, and Mn-α-Fe_2O_3/CuO/Ag films with the inset disclosing the modeled equivalent circuit used in fitting the raw EIS data: (b) and (c) presents the Bode plots of log |Z| vs. log frequency (Log F) and phase vs. Log F for the samples respectively.

Table 1. Evaluated values for the circuit elements used to model the EIS data obtained for the prepared Mn-α-Fe_2O_3, Mn-α-Fe_2O_3/CuO, and Mn-α-Fe_2O_3/CuO/Ag electrodes.

Sample	Rs	CPE-1		C1	Rbk	CPE-2		C2	Rct
	(Ω)	T (mF)	n1	(mF)	(kΩ)	T (mF)	n2	(mF)	(kΩ)

Mn-α-Fe_2O_3	9.76	0.058	0.85	0.04	1.79	0.12	0.93	0.15	195.1
Mn-α-Fe_2O_3/CuO	8.56	0.139	0.81	0.09	0.95	0.21	0.78	0.26	10.10
Mn-α-Fe_2O_3/CuO/Ag	9.92	0.210	0.75	0.12	0.83	0.40	0.76	0.55	7.00

The resistance, Rs, produces comparable values for all the electrodes in the range of 8.56 - 9.92 Ω as anticipated. This is because Rs is the series combination of the ionic resistance in the electrolyte, the resistance at the FTO contact, and the resistance in the external wires, which are similar for all the samples. The resistance of the trap states in the bulk of the Mn-α-Fe_2O_3/CuO electrodes significantly reduces by 46.9 % after the deposition of CuO films. This was caused by the in-built electric field formed at the interface of the junction between the two semiconductors, which boosted the mobility and transport of charge carriers [46]. The Rbk further drops by 6.7 % upon modification with plasmonic Ag NPs. The capacitance, C1, in the bulk of the electrodes, increased for the heterostructures by more than twice the value attained by Mn-α-Fe_2O_3. The capacitance of the surface states, C2, was enhanced by 73.0 % and 260 % for Mn-α-Fe_2O_3/CuO and Mn-α-Fe_2O_3/CuO/Ag films respectively, when compared to the value deduced for Mn-α-Fe_2O_3 samples. The resistance to the transfer of charges at the film's surface, Rct, observed for Mn-α-Fe_2O_3/CuO and Mn-α-Fe_2O_3/CuO/Ag heterostructures was over 19 and 27 times lower than the value obtained for Mn-α-Fe_2O_3 films, respectively. The in-built electric field between the two semiconductors boosted charge mobility and injection to the material's surface, which enhanced the electromagnetic field around the charges, increasing the capacitance in the bulk and surface of the films, while lowering the Rct values [74]. More so, for Mn-α-Fe_2O_3/CuO/Ag electrodes, the plasmonic effects of AgNPs further improved its impedance response and produced the least Rct value. The improved impedance response observed for the heterostructures will be relevant in

many photo-based applications such as photodetection, photovoltaic, and photoelectrocatalysis, which require reduced recombination of charge carriers and improved charge transport properties.

Bode plots extracted from the EIS data were further analysed to extract complementary information on the impedance response of the Mn-α-Fe_2O_3 and heterostructured samples. The plots of log |Z| vs. Log F and phase vs. Log F are disclosed in **Fig. 9 (b)** and **(c)** for the fabricated materials, respectively. The smallest log |Z| magnitude value, 3.6 Ω, was attained by Mn-α-Fe_2O_3/CuO/Ag electrodes followed by Mn-α-Fe_2O_3/CuO. This is an indication of a decrease in the resistance to charge transfer at the electrode/liquid junction of the heterostructures. Similarly, the phase vs. Log |Z| plots produced the least negative phase angle for the Mn-α-Fe_2O_3/CuO/Ag electrode, with Mn-α-Fe_2O_3 yielding the maximum value. A reduced negative phase angle value implies an improvement in the mobility of charge carriers and effective separation of charges around the electrode/liquid region [75]. These observations agree well with the analysis of the Nyquist plots of the samples and further affirm the improved impedance response of the heterostructured materials.

1.4 Conclusions

This project presents a porous Mn-α-Fe_2O_3/CuO/Ag heterostructure, fabricated using facile and cost-effective solution-based methods. The microstructural and optical properties of the heterostructures were investigated, and their impedance response was studied in an electrochemical system. The Mn-doped α-Fe_2O_3 films were deposited on FTO substrates in an electrodeposition process using an aqueous solution containing $FeCl_3$, $MnCl_2.4H_2O$, and 10% PEG as the electrolyte. Subsequently, CuO films with large shallow pores were deposited on the Mn-α-Fe_2O_3 films in a facile dip-coating process, followed by surface modification with Ag NPs via a

simple drop-casting approach to obtain porous Mn-α-Fe_2O_3/CuO/Ag heterostructures. FESEM studies disclosed spherical nanoparticles with varying levels of particle agglomeration for the fabricated composite materials that formed the heterostructure. Shallow pores were observed on the surface of the deposited CuO on Mn-α-Fe_2O_3 samples, induced by the aging of the Cu-based precursor used for the film's deposition. The porosity of Mn-α-Fe_2O_3/CuO films was further sustained after surface modification with Ag NPs. EDS studies affirm the presence of all the constituent elements that make up the heterostructure, while XRD and Raman spectroscopy investigations confirmed the structural integrity of the materials. The indirect and direct bandgaps estimated for the Mn-α-Fe_2O_3/CuO/Ag heterostructures are 2.05 and 2.61 eV, which are 3.8 and 2.5% less than the values deduced for the Mn-α-Fe_2O_3 films, respectively. Mott-Schottky analysis showed an n-type semiconducting property for the Mn-α-Fe_2O_3 samples, which was retained after forming heterostructures with CuO and CuO/AgNPs. The charge transfer resistance at the surfaces of Mn-α-Fe_2O_3/CuO and Mn-α-Fe_2O_3/CuO/Ag heterostructures in an electrochemical system was over 19 and 27 times lower than the estimated value obtained for Mn-α-Fe_2O_3 films. This work showcases facile and low-cost solution-based techniques for fabricating porous Mn-α-Fe_2O_3/CuO/Ag heterostructures with suitable properties for photo-based and optoelectronic applications.

Acknowledgment

The authors acknowledge financial support from the University of Pretoria (UP), the externally funded UP postdoctoral fellowship program: grant cost center: A1E689, and the South African Research Chairs Initiative (SARCHI), UID; 115463.

References

[1] J. Huang, A. Jones, T.D. Waite, Y. Chen, X. Huang, K.M. Rosso, A. Kappler, M. Mansor, P.G. Tratnyek, H. Zhang, Fe (II) redox chemistry in the environment, Chem. Rev., 121 (2021) 8161-8233.

[2] C. Yilmaz, U. Unal, Single step synthesis of (α-Fe_2O_3) hematite films by hydrothermal electrochemical deposition, RSC Adv., 5 (2015) 16082-16088.

[3] G. Ren, Y. Sun, M. Sun, Y. Li, A. Lu, H. Ding, Visible light enhanced extracellular electron transfer between a hematite photoanode and Pseudomonas aeruginosa, Minerals, 7 (2017) 230.

[4] P. Katikaneani, A.K. Vaddepally, N. Reddy Tippana, R. Banavath, S. Kommu, Phase transformation of iron oxide nanoparticles from hematite to maghemite in presence of polyethylene glycol: application as corrosion resistant nanoparticle paints, J. Nanosci., 2016 (2016).

[5] M. Tadic, M. Panjan, Y. Lalatone, I. Milosevic, B.V. Tadic, J. Lazovic, Magnetic properties, phase evolution, hollow structure and biomedical application of hematite (α-Fe_2O_3) and QUAIPH, Adv. Powder Technol., 33 (2022) 103847.

[6] A.C. Catto, S. Bernardini, K. Aguir, E. Longo, L.F. da Silva, In-situ hydrothermal synthesis of oriented hematite nanorods for sub-ppm level detection of ozone gas, J. Alloys Compd., 947 (2023) 169444.

[7] J. Talibawo, P.I. Kyesmen, M.C. Cyulinyana, M. Diale, Facile Zn and Ni Co-doped hematite nanorods for efficient photocatalytic water oxidation, Nanomaterials, 12 (2022) 2961.

[8] A.A. Qureshi, S. Javed, A. Fakharuddin, M.A. Akram, L. Schmidt-Mende, Low-temperature processed natural hematite as an electron extraction layer for efficient and stable perovskite solar cells, Surf. Interfaces, (2023) 103003.

[9] M.H. Lee, J.H. Park, H.S. Han, H.J. Song, I.S. Cho, J.H. Noh, K.S. Hong, Nanostructured Ti-doped hematite (α-Fe_2O_3) photoanodes for efficient photoelectrochemical water oxidation, Int. J. Hydrogen Energy, 39 (2014) 17501-17507.

[10] L. Xi, K.M. Lange, Surface modification of hematite photoanodes for improvement of photoelectrochemical performance, Catalysts, 8 (2018) 497.

[11] S.Y. Chiam, M.H. Kumar, P.S. Bassi, H.L. Seng, J. Barber, L.H. Wong, Improving the efficiency of hematite nanorods for photoelectrochemical water splitting by doping with manganese, ACS Appl. Mater. Interfaces, 6 (2014) 5852-5859.

[12] E.L. Tsege, T.S. Atabaev, M.A. Hossain, D. Lee, H.-K. Kim, Y.-H. Hwang, Cu-doped flower-like hematite nanostructures for efficient water splitting applications, J. Phys. Chem. Solids, 98 (2016) 283-289.

[13] A.S. Mokrushin, Y.M. Gorban, A.A. Averin, P.Y. Gorobtsov, N.P. Simonenko, Y.Y. Lebedinskii, E.P. Simonenko, N.T. Kuznetsov, Obtaining of ZnO/Fe_2O_3 thin nanostructured films by AACVD for detection of ppb-concentrations of NO_2 as a biomarker of lung infections, Biosensors, 13 (2023) 445.

[14] A. Tofanello, A.L. Freitas, W.M. Carvalho Jr, T. Salminen, T. Niemi, F.L. Souza, Hematite surface modification toward efficient sunlight-driven water splitting activity: the role of gold nanoparticle addition, J. Phys. Chem. C, 124 (2020) 6171-6179.

[15] A. Annamalai, P.S. Shinde, T.H. Jeon, H.H. Lee, H.G. Kim, W. Choi, J.S. Jang, Fabrication of superior α-Fe_2O_3 nanorod photoanodes through ex-situ Sn-doping for solar water splitting, Sol. Energy Mater. Sol. Cells, 144 (2016) 247-255.

[16] S. Zhang, J. Huang, X. Wu, W. Leng, H. Lu, X. Xu, D. Wu, Enhanced PPCP electrooxidation in pharmaceutical wastewater by cocatalyst modification over Ti-doped α-Fe_2O_3 electrodes, Chem. Eng. J., 474 (2023) 145523.

[17] S.K. Sarma, R. Mohan, A. Shukla, Structural, opto-electronic and photoelectrochemical properties of tin doped hematite nanoparticles for water splitting, Materials Science in Semiconductor Processing, 108 (2020) 104873.

[18] N.M. Ito, W.M. Carvalho, D.N.F. Muche, R.H.R. Castro, G.M. Dalpian, F.L. Souza, High temperature activation of hematite nanorods for sunlight driven water oxidation reaction, PCCP, 19 (2017) 25025-25032.

[19] H. Mei, S. Zhou, M. Lu, Y. Zhao, L. Cheng, Construction of pine-branch-like α-Fe_2O_3/TiO_2 hierarchical heterostructure for gas sensing, Ceram. Int., 46 (2020) 18675-18682.

[20] J. Ma, Q. Wang, L. Li, X. Zong, H. Sun, R. Tao, X. Fan, Fe_2O_3 nanorods/CuO nanoparticles pn heterojunction photoanode: Effective charge separation and enhanced photoelectrochemical properties, J. Colloid Interface Sci., 602 (2021) 32-42.

[21] M.R. Khan, T.W. Chuan, A. Yousuf, M. Chowdhury, C.K. Cheng, Schottky barrier and surface plasmonic resonance phenomena towards the photocatalytic reaction: study of their mechanisms to enhance photocatalytic activity, Catal. Sci. Technol., 5 (2015) 2522-2531.

[22] P. Zhang, T. Wang, J. Gong, Mechanistic understanding of the plasmonic enhancement for solar water splitting, Adv. Mater., 27 (2015) 5328-5342.

[23] P. Peerakiatkhajohn, J.H. Yun, H. Chen, M. Lyu, T. Butburee, L. Wang, Stable hematite nanosheet photoanodes for enhanced photoelectrochemical water splitting, Adv. Mater., 28 (2016) 6405-6410.

[24] A.M. Huerta-Flores, G. Chávez-Angulo, O.A. Carrasco-Jaim, L.M. Torres-Martínez, M. Garza-Navarro, Enhanced photoelectrochemical water splitting on heterostructured α-Fe_2O_3-TiO_2: X (X= Co, Cu, Bi) photoanodes: Role of metal doping on charge carrier dynamics improvement, J. Photochem. Photobiol. A: Chem., 410 (2021) 113077.

[25] R.B. Mammar, L. Hamadou, Highly broadband plasmonic Pt nanoparticles modified α-Fe_2O_3/TiO_2 nanotubes for efficient photoelectrochemical water splitting, Opt. Mater., 143 (2023) 114191.

[26] Z. Masoumi, M. Tayebi, M. Kolaei, B.-K. Lee, Unified surface modification by double heterojunction of MoS_2 nanosheets and $BiVO_4$ nanoparticles to enhance the photoelectrochemical water splitting of hematite photoanode, J. Alloys Compd., 890 (2022) 161802.

[27] S.A. Mahmoud, L.G. Amin, A.A. Akl, A. Dhahri, Investigation of linear and non-linear optical features of crystalline and non-crystalline iron oxide thin films for optoelectronic purposes, Physica B: Condensed Matter, 668 (2023) 415249.

[28] N. Abid, A.M. Khan, S. Shujait, K. Chaudhary, M. Ikram, M. Imran, J. Haider, M. Khan, Q. Khan, M. Maqbool, Synthesis of nanomaterials using various top-down and bottom-up

approaches, influencing factors, advantages, and disadvantages: A review, Adv. Colloid Interface Sci., 300 (2022) 102597.

[29] I. Rodríguez-Gutiérrez, K.C. Bedin, B. Mouriño, J.B. Souza Junior, F.L. Souza, Advances in Engineered Metal Oxide Thin Films by Low-Cost, Solution-Based Techniques for Green Hydrogen Production, Nanomaterials, 12 (2022) 1957.

[30] A.A. Akl, Influence of preparation conditions on the dispersion parameters of sprayed iron oxide thin films, Appl. Surf. Sci., 256 (2010) 7496-7503.

[31] C. Ji, J. Xu, Q. Jiang, G. Kerherve, H. Zhou, X. Li, S. Tang, P. Sharma, D.J. Riley, F. Xie, Significantly boosted photoelectrochemical water splitting performance by plasmonic enhanced Hematite@ MOF composite photoelectrodes, Mater. Today Adv., 18 (2023) 100361.

[32] M. Khalifa, M.H. Jaduaa, A.N. Abd, Quantum dots gold nanoparticles/porous silicon/silicon for solar cell applications, Mater. Today: Proc., 45 (2021) 5809-5814.

[33] N.D. Mosalakgotla, P.I. Kyesmen, M. Diale, Optimization of the processing parameters for the preparation of dip-coated CuO photocathodes and modification with Au nanoparticles for water-splitting, Mater. Chem. Phys., (2023) 127378.

[34] A.S. Nugraha, O. Guselnikova, J. Henzie, J. Na, M.S.A. Hossain, O.m. Dag, A.E. Rowan, Y. Yamauchi, Symmetry-breaking plasmonic mesoporous gold nanoparticles with large pores, Chem. Mater., 34 (2022) 7256-7270.

[35] P. Kumar, K.-H. Kim, K. Vellingiri, P. Samaddar, P. Kumar, A. Deep, N. Kumar, Hybrid porous thin films: Opportunities and challenges for sensing applications, Biosens. Bioelectron., 104 (2018) 120-137.

[36] S. Kumar, K. Ojha, A.K. Ganguli, Interfacial charge transfer in photoelectrochemical processes, Adv. Mater. Interfaces, 4 (2017) 1600981.

[37] A. Kleiman-Shwarsctein, Y.-S. Hu, A.J. Forman, G.D. Stucky, E.W. McFarland, Electrodeposition of α-Fe_2O_3 doped with Mo or Cr as photoanodes for photocatalytic water splitting, J. Phys. Chem. C, 112 (2008) 15900-15907.

[38] P.I. Kyesmen, N. Nombona, M. Diale, Influence of coating techniques on the optical and structural properties of hematite thin films, Surf. Interfaces, 17 (2019) 100384.

[39] P.I. Kyesmen, N. Nombona, M. Diale, Tuning the Surface Properties of CuO Films Using the Precursor Aging Approach for Enhanced Photoelectrocatalytic Reactions, Adv. Mater. Interfaces, (2023) 2300230.

[40] R.C. Doty, T.R. Tshikhudo, M. Brust, D.G. Fernig, Extremely stable water-soluble Ag nanoparticles, Chem. Mater., 17 (2005) 4630-4635.

[41] A.G. Tamirat, A.A. Dubale, W.-N. Su, H.-M. Chen, B.-J. Hwang, Sequentially surface modified hematite enables lower applied bias photoelectrochemical water splitting, PCCP, 19 (2017) 20881-20890.

[42] A. Goktas, S. Modanlı, A. Tumbul, A. Kilic, Facile synthesis and characterization of ZnO, ZnO: Co, and ZnO/ZnO: Co nano rod-like homojunction thin films: Role of crystallite/grain size and microstrain in photocatalytic performance, J. Alloys Compd., 893 (2022) 162334.

[43] L.G. Devi, N. Kottam, S.G. Kumar, Preparation and characterization of Mn-doped titanates with a bicrystalline framework: correlation of the crystallite size with the synergistic effect on the photocatalytic activity, J. Phys. Chem. C, 113 (2009) 15593-15601.

[44] D. Gygi, E.D. Bloch, J.A. Mason, M.R. Hudson, M.I. Gonzalez, R.L. Siegelman, T.A. Darwish, W.L. Queen, C.M. Brown, J.R. Long, Hydrogen storage in the expanded pore metal–organic frameworks M2 (dobpdc)(M= Mg, Mn, Fe, Co, Ni, Zn), Chem. Mater., 28 (2016) 1128-1138.

[45] K. Sivula, F. Le Formal, M. Grätzel, Solar water splitting: progress using hematite (α-Fe_2O_3) photoelectrodes, ChemSusChem, 4 (2011) 432-449.

[46] S. Bai, J. Liu, M. Cui, R. Luo, J. He, A. Chen, Two-step electrodeposition to fabricate the p–n heterojunction of a $Cu_2O/BiVO_4$ photoanode for the enhancement of photoelectrochemical water splitting, Dalton Trans., 47 (2018) 6763-6771.

[47] W.L. Oliani, D.F. Parra, L.G.H. Komatsu, N. Lincopan, V.K. Rangari, A.B. Lugao, Fabrication of polypropylene/silver nanocomposites for biocidal applications, Mater. Sci. Eng. C, 75 (2017) 845-853.

[48] I.Y. Kaplin, E.S. Lokteva, S.V. Bataeva, K.I. Maslakov, A.V. Fionov, A.V. Shumyantsev, O.Y. Isaikina, A.O. Kamaev, E.V. Golubina, Effect of MnO_x modification and template type on

the catalytic performance of ceria-zirconia in CO and soot oxidation, Pure Appl. Chem., 93 (2021) 447-462.

[49] S. Krehula, M. Ristić, Ž. Petrović, L.K. Krehula, I. Mitar, S. Musić, Effects of Cu doping on the microstructural, thermal, optical and photocatalytic properties of α-FeOOH and α-Fe_2O_3 1D nanoparticles, J. Alloys Compd., 802 (2019) 290-300.

[50] S. Krehula, M. Ristić, M. Reissner, S. Kubuki, S. Musić, Synthesis and properties of indium-doped hematite, J. Alloys Compd., 695 (2017) 1900-1907.

[51] R. Nithiyavathi, S.J. Sundaram, G.T. Anand, D.R. Kumar, A.D. Raj, D.A. Al Farraj, R.M. Aljowaie, M.R. AbdelGawwad, Y. Samson, K. Kaviyarasu, Gum mediated synthesis and characterization of CuO nanoparticles towards infectious disease-causing antimicrobial resistance microbial pathogens, J. Infect. Public Health, 14 (2021) 1893-1902.

[52] P. Nunes, E. Fortunato, P. Tonello, F.B. Fernandes, P. Vilarinho, R. Martins, Effect of different dopant elements on the properties of ZnO thin films, Vacuum, 64 (2002) 281-285.

[53] Y. Zhang, J. Yan, Q. Li, C. Qu, L. Zhang, W. Xie, Optical and structural properties of Cu-doped β-Ga_2O_3 films, Mater. Sci. Eng. B, 176 (2011) 846-849.

[54] P.I. Kyesmen, N. Nombona, M. Diale, Modified annealing approach for preparing multi-layered hematite thin films for photoelectrochemical water splitting, Mater. Res. Bull., 131 (2020) 110964.

[55] L.-X. Zhang, M.-M. Zhao, Y.-Y. Yin, Y. Xing, L.-J. Bie, Rich defects and nanograins boosted formaldehyde sensing performance of mesoporous polycrystalline ZnO nanosheets, Rare Met., 41 (2022) 2292-2304.

[56] P.I. Kyesmen, N. Nombona, M. Diale, A Promising Three-Step Heat Treatment Process for Preparing CuO Films for Photocatalytic Hydrogen Evolution from Water, ACS omega, 6 (2021) 33398-33408.

[57] N. Pattanayak, P. Panda, S. Parida, Al doped hematite nanoplates: structural and Raman investigation, Ceram. Int., 48 (2022) 7636-7642.

[58] J. Wang, J. Zhao, Y. Li, M. Yang, Y.-Q. Chang, J.-P. Zhang, Z. Sun, Y. Wang, Enhanced light absorption in porous particles for ultra-NIR-sensitive biomaterials, ACS Macro Lett., 4 (2015) 392-397.

[59] L.A. Marusak, R. Messier, W.B. White, Optical absorption spectrum of hematite, αFe_2O_3 near IR to UV, J. Phys. Chem. Solids, 41 (1980) 981-984.

[60] S.Y. Chae, G. Rahman, O.-s. Joo, Elucidation of the structural and charge separation properties of titanium-doped hematite films deposited by electrospray method for photoelectrochemical water oxidation, Electrochim. Acta, 297 (2019) 784-793.

[61] S.C. Qi, X.Y. Qian, Q.X. He, K.J. Miao, Y. Jiang, P. Tan, X.Q. Liu, L.B. Sun, Generation of hierarchical porosity in metal–organic frameworks by the modulation of cation valence, Angew. Chem. Int. Ed., 58 (2019) 10104-10109.

[62] F.L. Souza, K.P. Lopes, P.A. Nascente, E.R. Leite, Nanostructured hematite thin films produced by spin-coating deposition solution: Application in water splitting, Sol. Energy Mater. Sol. Cells, 93 (2009) 362-368.

[63] P.R. Jubu, E. Danladi, H. Chahul, A. Aldayyat, Y. Yusof, K.M. Chahrour, P. Kyesmen, M. Tyona, L. Abiem, F. Yam, Photoanodic properties of In/β-Ga_2O_3 nanostructures fabricated under hydrogen reducing ambient by the vapour-phase growth method, Opt. Mater., 145 (2023) 114424.

[64] H. Wang, J.A. Turner, Characterization of hematite thin films for photoelectrochemical water splitting in a dual photoelectrode device, J. Electrochem. Soc., 157 (2010) F173-F178.

[65] Y. Liang, C.S. Enache, R. van de Krol, Photoelectrochemical Characterization of Sprayed [alpha]-Fe_2O_3 Thin Films: Influence of Si Doping and SnO_2 Interfacial Layer, Int. J. Photoenergy, 2008 (2008).

[66] Y. Zhang, W. Li, Z. Sun, Q. Zhang, L. Wang, Z. Chen, In-situ synthesis of heterostructured $BiVO_4$/BiOBr core-shell hierarchical mesoporous spindles with highly enhanced visible-light photocatalytic performance, J. Alloys Compd., 713 (2017) 78-86.

[67] C. Hao, W. Wang, R. Zhang, B. Zou, H. Shi, Enhanced photoelectrochemical water splitting with TiO_2@Ag_2O nanowire arrays via pn heterojunction formation, Sol. Energy Mater. Sol. Cells, 174 (2018) 132-139.

[68] P. Shinde, A. Punde, S. Shah, A. Waghmare, Y. Hase, B. Bade, V. Doiphode, S. Ladhane, S. Rahane, D. Kale, Plasmonic Au nanoparticles sensitized ZnO/CuO heterostructure for efficient photoelectrochemical water splitting, Int. J. Hydrogen Energy, 54 (2024) 1073-1084.

[69] Y. Kumar, R. Kumar, P. Raizada, A.A.P. Khan, A. Singh, Q. Van Le, V.-H. Nguyen, R. Selvasembian, S. Thakur, P. Singh, Current status of hematite (α-Fe_2O_3) based Z-scheme photocatalytic systems for environmental and energy applications, Journal of Environmental Chemical Engineering, 10 (2022) 107427.

[70] R.O. Mhadi, R.A. Ismail, M.H. Mohsin, Fabrication of high photosensitivity nanostructured n-Fe_2O_3/p-Si heterojunction photodetector by rapid thermal oxidation of chemically sprayed FeS_2 film, Materials Research Express, 6 (2019) 126202.

[71] E. Aguilera-Ruiz, M. De La Garza-Galván, P. Zambrano-Robledo, J. Ballesteros-Pacheco, J. Vazquez-Arenas, J. Peral, U. García-Pérez, Facile synthesis of visible-light-driven Cu_2O/$BiVO_4$ composites for the photomineralization of recalcitrant pesticides, RSC Adv. 7 (2017) 45885–45895, in.

[72] J. Sun, L. Sun, X. Yang, S. Bai, R. Luo, D. Li, A. Chen, Photoanode of coupling semiconductor heterojunction and catalyst for solar PEC water splitting, Electrochim. Acta, 331 (2020) 135282.

[73] B. Hirschorn, M.E. Orazem, B. Tribollet, V. Vivier, I. Frateur, M. Musiani, Determination of effective capacitance and film thickness from constant-phase-element parameters, Electrochim. Acta, 55 (2010) 6218-6227.

[74] K. Natarajan, M. Saraf, S.M. Mobin, Visible-light-induced water splitting based on a novel α-Fe_2O_3/CdS heterostructure, ACS omega, 2 (2017) 3447-3456.

[75] A. Mahmood, F. Tezcan, G. Kardaş, Photoelectrochemical characteristics of CuO films with different electrodeposition time, Int. J. Hydrogen Energy, 42 (2017) 23268-23275.